Fe$_3$Se$_4$/FeSe heterojunctions in cornstalk-derived N-doped carbon framework enhance charge transfer and cathodic oxygen reduction reaction to boost bio-electricity generation

Baojian Jing[a], Shijie You[b], Yuanyuan Ma[a], Zipeng Xing[a], Hun Chen[a], Ying Dai[a,c,*], Chunyue Zhang[a], Nanqi Ren[b], Jinlong Zou[a,*]

[a] Key Laboratory of Functional Inorganic Material Chemistry, Ministry of Education of the People's Republic of China, School of Chemistry and Materials Science, Heilongjiang University, Harbin, 150080, China
[b] State Key Laboratory of Urban Water Resource and Environment, School of Environment, Harbin Institute of Technology, Harbin, 150090, China
[c] School of Civil Engineering, Heilongjiang Institute of Technology, Harbin, 150050, China

ABSTRACT

Sluggish kinetics of oxygen reduction reaction (ORR) on air-cathode of microbial fuel cells (AC-MFCs) is one of the main obstacles for energy loss. In this study, nitrogen-doped Fe$_3$Se$_4$/FeSe/partially-graphitized carbon (Fe$_3$Se$_4$/FeSe/NPGC) composites as non-precious-metal air-cathode (ORR) catalysts are obtained using waste biomass (cornstalk cores) as raw material. As carbonization temperature increases (800–950 °C), the crystalline phase transition between Fe$_3$Se$_4$ and FeSe is strengthened to form the Fe$_3$Se$_4$/FeSe heterojunctions. The highest power density (1003 mW m^{-2}) and durability (decline of 7.8% after 105 d operation) are obtained by Fe$_3$Se$_4$/FeSe/NPGC (850 °C) cathode in AC-MFCs, which are higher than those of Pt/C (840 mW m^{-2}, 52.4%). The high ORR activity of Fe$_3$Se$_4$/FeSe/NPGC (850 °C) is partly attributed to the large specific surface area (356.68 m^2 g^{-1}) and porous structure. Doped N atoms (pyridinic N, pyrrolic N and graphitic N) in carbon skeleton enhance the charge delocalization of C atoms to reduce the electron loss to enhance the electron utilization via a four-electron (4e$^-$) ORR pathway. Fe$_3$Se$_4$/FeSe heterojunctions should greatly promote the charge transfer and oxygen dissociation efficiencies. The highly-conductive NPGC skeleton also contributes to the efficient charge transfer. The good long-term durability of AC-MFCs with Fe$_3$Se$_4$/FeSe/NPGC (850 °C) cathode is mainly ascribed to its fast ORR kinetics, which still generates a small amount (below 10.0%) of H$_2$O$_2$ (•OH and •O$_2$$^-$) intermediate to inhibit the electrogenic microbe growth on cathode surface. This work not only provides the fundamental studies on carbon-supported transition-metal selenides for ORR, but also provides a new kind of promising alternatives for precious metal-based electrodes for AC-MFCs.

1. Introduction

With the energy crisis and environmental pollution, the development of new clean energy is of great importance, especially for China [1,2]. Microbial fuel cells (MFCs) including air-cathode MFC (AC-MFC) have been generally recognized as sustainable energy technologies for wastewater treatment [3–8]. Microorganisms produce protons and electrons by degrading organic matters in wastewater [9,10]. Electrons are delivered to the cathode through external circuitry simultaneously with the protons transport in the medium [9,11,12]. The slow reaction kinetics of cathodic oxygen reduction reaction (ORR) and the poor tolerance of cathode material have become the main factors restricting the development of MFCs [13–15]. The microbes will be attached to the

cathode surface of AC-MFC to affect the electron/proton flow (especially for Pt-based catalysts), which decrease the ORR activity of the catalysts and the long-term operation durability [16–18]. Moreover, due to the high cost of Pt-based catalysts, recent studies are mainly focused on finding the alternative ORR catalysts [19]. Therefore, finding a high-performance and durable cathode catalyst has become the key factor for AC-MFC development [11,20].

Note that Pt-based catalyst usually exhibits a high over-potential during the ORR in AC-MFC, because the active sites of Pt are very easily invalidated by the pollutants (toxicant) in wastewater [21]. Recent studies have indicated that carbon-based or carbon-metals (including metal compounds)-based (M/C) catalysts have been widely used as cathode catalysts for ORR in AC-MFC [1]. The properties exhibited by

M/C catalysts are well suited for AC-MFC [22,23]. The most important benefits of these catalysts are their high specific surface area and electrical conductivity [15,24,25]. Currently, the usually-used M/C catalysts include MoS_2/C [26], Fe/Fe_3C@C [27], Co_xSe_y/MWCNT [28], Fe/N/C [29], FeCo/NC [30], etc. Although the M/C catalysts have some advantages including the high stability and electrical conductivity, their high ORR over-potentials caused by low activity and durability still need to be overcome [18]. However, this leaves us the space to continue the related studies.

Some studies have reported that transition metal (including Fe [29], Co [31], Ni [32] and Mn [33]) compounds loaded on carbon supports show good catalytic performance for ORR. In recent studies, Fe-based compounds including FeS [34], Fe_3O_4 [34], FeP [35], FePc [14], etc, are usually used as the active components for electrocatalysis. Fe_3Se_4 has a NiAs-type structure, and the iron vacancies are arranged in an ordered fashion [36]. In the past, Fe_3Se_4 has been studied as permanent magnets for replacement of rare earth metals [37]. However, there are few reports on the electrochemical properties of Fe_3Se_4. Due to the ordered arrangement of iron vacancies in Fe_3Se_4, it may provide efficient active sites for ORR [36]. Interestingly, if the overlapping of exposed crystal faces of Fe_3Se_4 is efficiently limited to avoid the decrease of the surface energy, the catalytic activity of Fe_3Se_4 should be further enhanced [37,38]. Furthermore, recent study has found that FeSe mounted on a 3D hollow porous carbon framework has a good ORR property [39]. Therefore, we plan to modify the lattice structure of Fe_3Se_4 with FeSe and then apply Fe_3Se_4/FeSe to the air cathode of AC-MFC as active components for ORR.

In this study, the main strategy is to embed Fe_3Se_4 in carbon skeleton to control the growth of exposed crystal faces, meanwhile, to allow the existence of mixed crystal phases (Fe_3Se_4/FeSe) to obtain the promising stability/activity of Fe_3Se_4/FeSe heterojunctions. Therefore, N-doped Fe_3Se_4/FeSe/partly-graphitized carbon (Fe_3Se_4/FeSe/NPGCs) composites are prepared as the ORR catalysts. As we know, it is the first time to use Fe_3Se_4/FeSe/NPGCs as catalysts for electro-catalytic reaction, especially for AC-MFC. The effects of carbonization temperature (800–950 °C) on the structure evolution and crystalline phase transition of Fe_3Se_4/FeSe/NPGCs have been investigated. The Fe_3Se_4/FeSe heterojunctions in the NPGC skeleton should contribute to the exceptional stability of Fe_3Se_4/FeSe/NPGCs. The doped N atoms can substitute the C atoms in carbon chain to generate defects in PGC skeleton. The formed pyridinic N, pyrrolic N and graphitic N are considered as highly-active sites for improving ORR rate. The ORR pathway and long-time running (120 d) performances of Fe_3Se_4/FeSe/NPGC cathodes in AC-MFCs are also investigated. It is expected that the Fe_3Se_4/FeSe/NPGC catalysts with high ORR activity can replace the Pt-based catalysts in MFCs or other fuel cells.

2. Experimental section

2.1. Synthesis of Fe_3Se_4/FeSe/NPGC catalysts

The Fe_3Se_4/FeSe/NPGC catalysts were prepared via a simple one-pot reduction method (Scheme 1). The dried cornstalks were peeled to take the cornstalk cores, which were then cut into small pieces. The melamine with a mass ratio of melamine to cornstalk cores of 0.3: 1 was dissolved in deionized water. The cornstalk cores were soaked in the melamine solution for 12 h and then dried in a blast oven. 0.316 g of selenium powder and 4 mL hydrazine hydrate were mixed in a beaker and then stirred continuously until the solution (A) was no longer bubble. The solution A was poured into the $FeCl_3$ solution (the molar ratio of Fe: Se was 9:8) to obtain the solution B. The treated cornstalk cores were immersed in the solution B and then stirred in a water bath at 80 °C for 10 h. The mass ratio of selenium powder to treated cornstalk cores was 1: 10. After stirring, the mixture was dried at 80 °C and then carbonized at 800, 850, 900, and 950 °C for 2 h under N_2 flowing condition at a heating rate of 3 °C min^{-1}. The final samples were ground in an agate mortar, which were marked as Fe_3Se_4/FeSe/NPGC-x (x = 800, 850, 900 and 950).

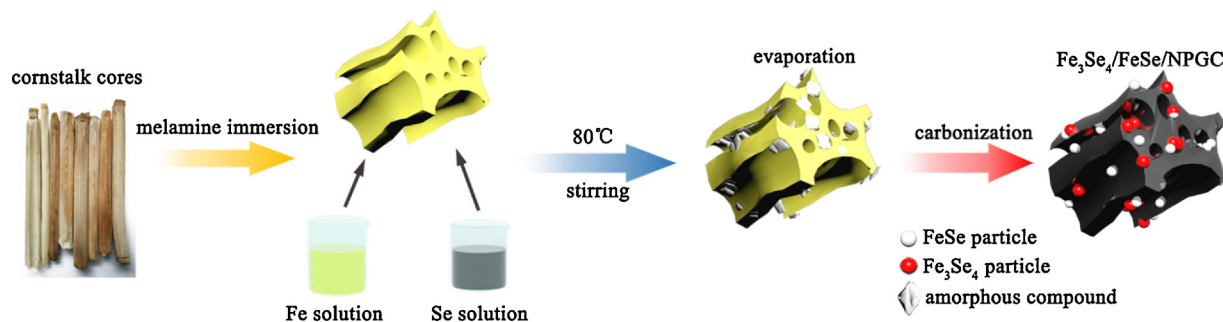### 2.2. Anode and cathode preparation for AC-MFC

Carbon fiber brush (CFB) was used as the anode for AC-MFC. The CFB was soaked in acetone for 24 h to remove residual impurities. The soaked CFB was dried and calcined in air at 450 °C for 30 min before use [40]. The cathode base material of AC-MFC was the 60 mesh stainless steel mesh. Carbon black and PTFE were mixed with a mass ratio of 7: 3, which was then rolled onto the stainless steel mesh as gas diffusion layer (GDL). The GDL was calcined in air at 340 °C for 30 min to obtain a higher stability [41]. The mixture of the prepared Fe_3Se_4/FeSe/NPGC-x (x = 800, 850, 900, and 950) and PTFE was rolled onto the other side of GDL, which was marked as catalyst layer with a projected area of 7 cm^2 [42]. Commercial Pt/C (10 wt%, Hesen Electric Co., Ltd, Shanghai, China) was used as a reference ORR catalyst for AC-MFC.

2.3. AC-MFC construction and operation

The AC-MFC was constructed with a 28 mL cylindrical plexiglas chamber (3 cm in diameter and 4 cm in length). The neutral electrolyte was consisted of phosphate-buffered saline (50 mM PBS) and glucose (1 g L^{-1}), as reported in previous studies [43]. The AC-MFC was run at 30 °C to ensure the smooth growth of the electrogenic microorganisms. During the operation, the external resistance was 1000 Ω, and the electrolyte was replaced every three days. The voltage output of AC-MFC was recorded by a data acquisition system (PISO-813, ICP-DAS, Taiwan). Power density, polarization curve, and Coulomb efficiency (CE) were measured by changing the external resistances. Chemical oxygen demand (COD) was measured using the fast digestion method [34]. To ensure the validity of the data, three reactors were parallel operated under the same condition.

2.4. Material characterization and analysis

X-ray diffraction (XRD) tests were implemented with a SmarkLab (9 KW) diffractometer (Japanese science). XRD patterns were analyzed

Scheme 1. Synthesis route for Fe_3Se_4/FeSe/NPGC composite.

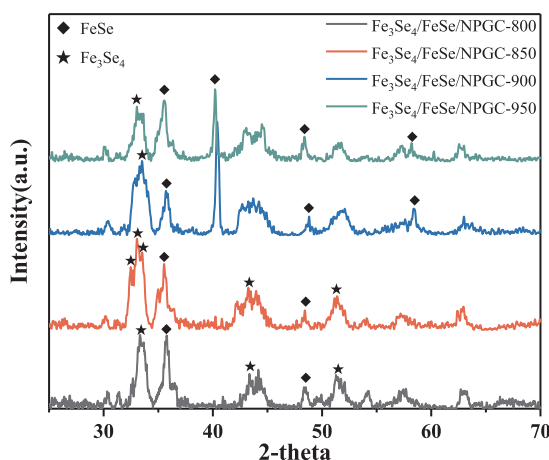**Fig. 1.** XRD patterns of Fe₃Se₄/FeSe/NPGC-x (x = 800, 850, 900 and 950).

according to the data of the Joint Commission on powder diffraction (JCPDS). X-ray photoelectron spectroscopy (XPS) was obtained on Kratos-AXISUL TRA DLD (Al Kα X-ray source). XPS data for each atom was fitted with the 'XPS peak' software. The N₂ adsorption/desorption isotherm was measured using a Micromeritics Tristar II at 77 K. The specific surface area (S$_{BET}$) was calculated by using the Brunauer-Emmett-Teller (BET) method; meanwhile, the pore size distribution was obtained using the Barrett-Joyner-Halenda (BJH) method. Scanning Electron Microscope (SEM) images were taken on an S-4800 scanning electron microscope (Japan). JEM-2100 electron microscope (JEOL) was used to obtain the Transmission Electron Microscopy (TEM) images to investigate the internal structure of Fe₃Se₄/FeSe/NPGCs.

2.5. Materials electrochemical analysis

Electrochemical tests were performed on a CHI760E electrochemical workstation (CH Instruments ChenHua Corp. Shanghai, China). The catalyst ink was prepared via ultrasonic dispersion of catalyst in the mixture of Nafion (50 μL) and ethanol (100 μL) for 30 min [11,26,35]. During the operation of AC-MFC, the electrochemical impedance spectroscopy (EIS) test was performed at an open circuit potential (OCP) in the frequency range of 10^5 to 10^{-2} Hz using a sinusoidal disturbance of 10 mV amplitude [43]. The reference electrode used a saturated calomel electrode (SCE). ZSimpWin 3.10 software (Echem, US) was used to fit the EIS data to calculate the charge transfer resistance (R$_{ct}$). Rotating disk electrode (RDE) test was conducted in an O₂-saturated 50 mM PBS at various rotation rates from 225 to 2025 rpm (5 mV s^{-1}). The Koutecky-Levich (K-L) plots (J^{-1} vs. $\omega^{-1/2}$) were obtained at the potentials of 0.3, 0.35 and 0.4 V, which were then fitted into the linear curves to calculate the electron transfer numbers (n) by using the following K-L Eq. (1) [44]:

$$\frac{1}{J} = \frac{1}{J_K} + \frac{1}{B\omega^{1/2}}$$

(1)

where J is the measured current density (mA cm^{-2}), J_K is the kinetic current density, and ω is the rotating rate (rpm). B is calculated from the slope of K-L plots based on the Eq. (2):

$$B = 0.2nFC_0D_0^{2/3}\nu^{-1/6}$$

(2)

where n is the number of electrons transferred per oxygen molecule, F is the Faraday constant (96485 C mol^{-1}), C_O is the bulk concentration of O₂ (1.2×10^{-6} mol cm^{-3}), D_O is the O₂ diffusion coefficient (1.9×10^{-5} cm^2 s^{-1}), and ν is the kinematic viscosity of the electrolyte (0.01 cm^2 s^{-1}). The constant of 0.2 is adopted when the rotation speed is expressed in rpm.

Rotating ring disk electrode (RRDE) tests were used to investigate the catalytic ORR kinetics of Fe₃Se₄/FeSe/NPGC-850 and Pt/C. The

obtained ink was dropped on the disk of glassy carbon electrode. The RRDE tests were performed in 50 mM PBS at a rotation rate of 1600 rpm with oxygen flow (5 mV s^{-1}). Before the tests, the electrolyte was fully saturated with oxygen for at least 30 min. The RRDE test obtained the current densities produced by the disk (j_D) and the ring (j_R) to quantify the intermediate (hydrogen peroxide, H₂O₂) and n [45]. The n value and H₂O₂ yield (%) were calculated using the following Eqs. (1) and (2), respectively.

$$n = \left| \frac{4 \times j_D}{j_D - j_R} \right|$$

(3)

$$H_2O_2[\%] = \frac{4-n}{2} \times 100$$

(4)

3. Results and discussion

3.1. Material characteristics and analyses

The crystalline phases of Fe₃Se₄/FeSe/NPGC catalysts at different carbonization temperature are investigated by XRD tests. As shown in Fig. 1, the broad peaks at around 33.136°, 43.113°, and 51.628° correspond to the (111), (311), and ($\bar{3}$ 13) crystal planes of bulk Fe₃Se₄ (JCPDS, NO.657252) in Fe₃Se₄/FeSe/NPGCs, respectively [46]. In addition, there are also four peaks at around 35.794°, 40.198°, 48.926°, and 58.924°, which are ascribed to the (111), (102), (201) and (202) crystal planes of FeSe, respectively [47]. The (102) and (202) crystal planes of FeSe can be only observed for Fe₃Se₄/NPGC-900 and Fe₃Se₄/NPGC-950. Note that the weak peaks at around 32.513° and 33.617° belong to the (002) and ($\bar{4}$ 02) lattice planes of Fe₃Se₄ in Fe₃Se₄/FeSe/NPGC-850. It indicates that the crystalline phase transition in Fe₃Se₄/FeSe/NPGCs is significantly influenced by the carbonization temperature. At 800 °C, the main crystalline phase is Fe₃Se₄, which is co-existed with a small amount of FeSe. As the temperature increases, the intensity of the main peak (33.136°) of Fe₃Se₄ increases, and the peaks of ($\bar{4}$ 02) and (311) crystal faces appear on both sides of the main peak. At 900 and 950 °C, two new peaks of the (102) and (202) crystal planes of FeSe are emerged. It implies that as temperature increases, the proportion of FeSe continuously increases, while the proportion of Fe₃Se₄ gradually decreases to form the different Fe₃Se₄/FeSe heterojunctions in Fe₃Se₄/FeSe/NPGCs. This interesting crystalline phase transition between Fe₃Se₄ and FeSe should endue the special functions to Fe₃Se₄/FeSe/NPGCs.

N₂ adsorption and desorption tests are performed for Fe₃Se₄/FeSe/NPGC-x (x = 800, 850, 900 and 950) (Fig. S1 and Table S1). As shown in Fig. S1, the isotherms belong to the type IV isotherm and the hysteresis loops belong to the H-3 type, indicating that the samples are mainly consisted of mesoporous structure [48]. Fe₃Se₄/FeSe/NPGC-850 has the largest S$_{BET}$ of 356.68 m^2 g^{-1}, which is much higher than those of the other three samples (283.02, 192.89 and 196.79 m^2 g^{-1}). S$_{BET}$ and pore volume of the samples become smaller as the temperature increases from 850 to 950 °C (Table S1), indicating that the intrinsic pore structure of cornstalk cores should gradually collapse and meanwhile the Fe₃Se₄/FeSe crystals may grow up to block the pores. Generally, a large S$_{BET}$ can provide more active sites on the surface of the catalyst, and provide more pore channels for efficient transport of oxygen (O₂, as the electron acceptor). Therefore, Fe₃Se₄/FeSe/NPGC-850 with the highest S$_{BET}$ may facilitate the smooth supply and reaction of available O₂ on the active sites in the porous structure to improve the ORR efficiency.

XPS spectra of Fe₃Se₄/FeSe/NPGC-x (x = 800, 850, 900 and 950) are shown in Fig. 2a. Five elements (C, N, Fe, Se and O) are detected on the surface of Fe₃Se₄/FeSe/NPGCs. The main peaks centered at around 284.6 and 532.0 eV refer to the C 1 s and O 1 s, respectively [26]. The peaks at around 400.0 eV can be assigned to the N 1 s [26]. In addition, the peaks of Fe 2p and Se 3d are observed at around 710.0 and 58.0 eV,
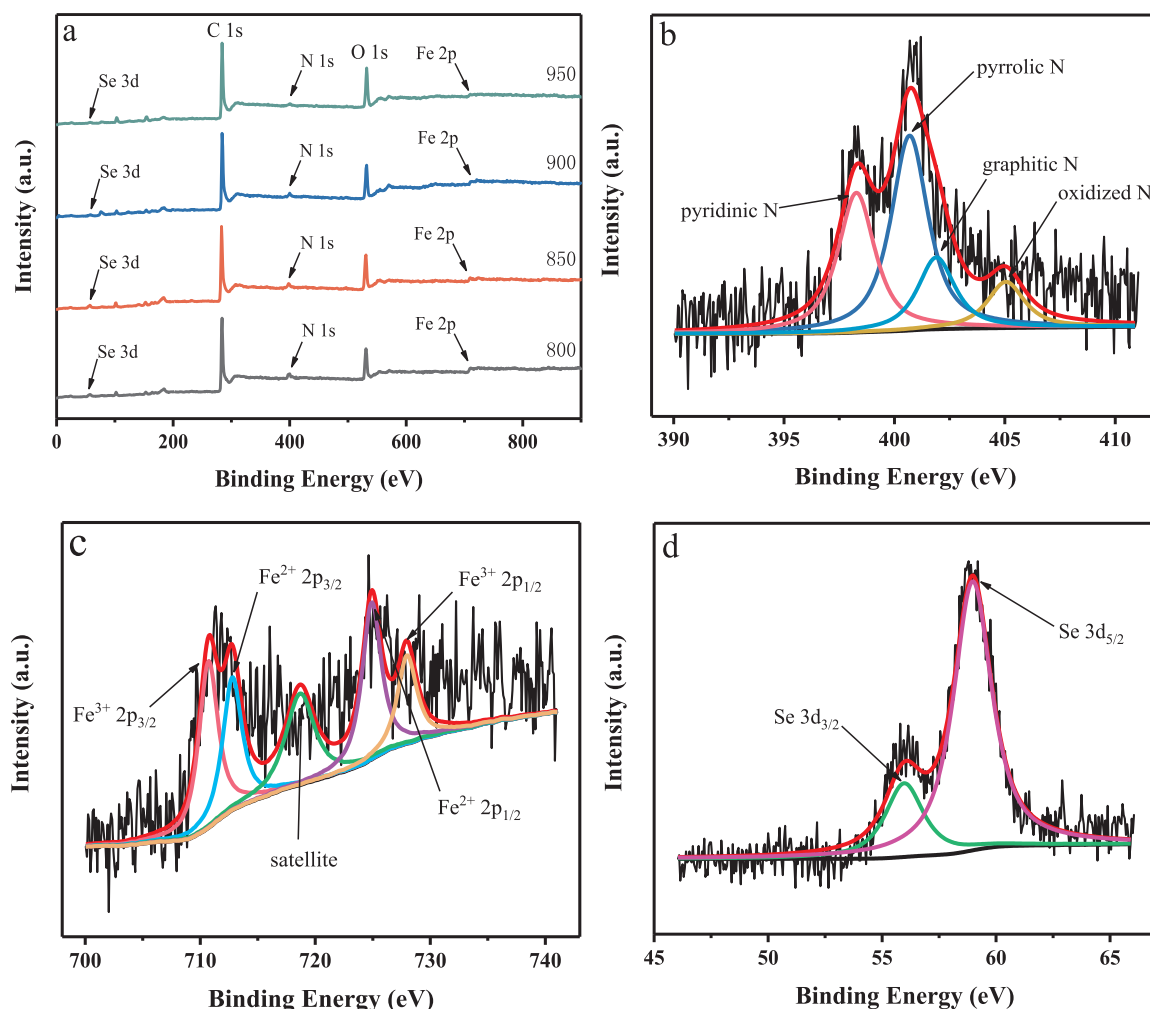
Fig. 2. XPS survey spectra (a) for Fe_3Se_4/FeSe/NPGC-x (x = 800, 850, 900 and 950) and high resolution XPS of Fe_3Se_4/FeSe/NPGC-850 (b-N 1 s, C-Fe 2p and d-Se 3d).

respectively [26,44], confirming that the Fe_3Se_4/FeSe particles are successfully incorporated into the NPGC skeleton, consistent with the XRD results. As illustrated in Fig. S2 (a − d), the C 1 s spectra of Fe_3Se_4/FeSe/NPGCs can be deconvoluted into three components, which can be identified as graphitic C (around 284.6 eV), C − N (around 285.9 eV), and C − O (around 287 eV) [34]. Note that the graphitization of bio-mass carbon can help to increase the electrical conductivity of the catalyst, which is critical to the acceleration of electron transfer during the ORR. Furthermore, a large number of defects should be existed on the carbon skeleton by introducing N species and Fe_3Se_4/FeSe hetero-junctions to the PGC.

As shown in Fig. 2b and Fig. S2 (e − g), the N 1 s spectra can be deconvolved into four characteristic peaks at around 398.1, 400.5, 401.9, and 405 eV, which correspond to pyridinic N, pyrrolic N, gra-phitic N, and oxidized N, respectively [49]. As mentioned in previous study, the heteroatom N doped in NPGC plays a key role in the ORR process [22]. Pyridinic N, pyrrolic N and graphitic N have the positive effects on the ORR process [22]. In addition, the bonds between O and N atoms can promote the chemisorption of oxygen molecules (O_2) and intermediates by adjacent C atoms [19]. The incorporation of N atoms into carbon rings leads to the charge delocalization of C atoms to contribute to the high electrical conductivity and the efficient activa-tion of oxygen [34]. As the temperature increases, the percentage contents of graphitic N and oxidized N gradually increase (as shown in Table 1). This result implies that pyridinic N may be converted to graphitic N and oxidized N as temperature increases. As previously

Table 1
Percentage contents (at. %) of various chemical states of N in Fe_3Se_4/FeSe/NPGC-x (x = 800, 820, 900 and 950).

samples	Pyridinic N	Pyrrolic N	Graphitic N	Oxidized N
Fe_3Se_4/FeSe/NPGC-800	41.17	45.51	10.41	2.91
Fe_3Se_4/FeSe/NPGC-850	30.86	43.07	15.86	10.21
Fe_3Se_4/FeSe/NPGC-900	24.59	48.54	16.65	10.23
Fe_3Se_4/FeSe/NPGC-950	14.01	44.09	27.69	14.22

reported, pyrrolic N is stable and less affected by pyrolysis temperature [34]. Because pyridinic N has a lone electron in the plane of the carbon matrix, it can improve the electron supply ability of the catalyst during ORR [22]. Both pyridinic N and graphitic N can provide the highly active sites to enhance the disassociation of O=O bond by inducing uneven electronic distribution.

The Fe 2p spectra (Fig. 2c and Fig. S2 (h–j)) can be fitted to two asymmetric resolved doublets resulting from the spin-orbit splitting, which are assigned to Fe $2p_{3/2}$ at lower binding energy and Fe $2p_{1/2}$ at higher binding energy. The peaks of Fe 2p at a lower binding energy can be divided into two components including Fe(III) $2p_{3/2}$ (around 710.8 eV) and Fe(II) $2p_{3/2}$ (around 713.0 eV) [50]. At higher binding energies, the peak can be divided into Fe(II) $2p_{1/2}$ (around 723.8 eV) and Fe(III) $2p_{1/2}$ (around 726.1 eV) [51]. The peak at around 717.7 eV is a satellite peak for the above four peaks [52]. It can be seen from the results that Fe(II) and Fe(III) are co-existed in the Fe_3Se_4/FeSe/NPGC

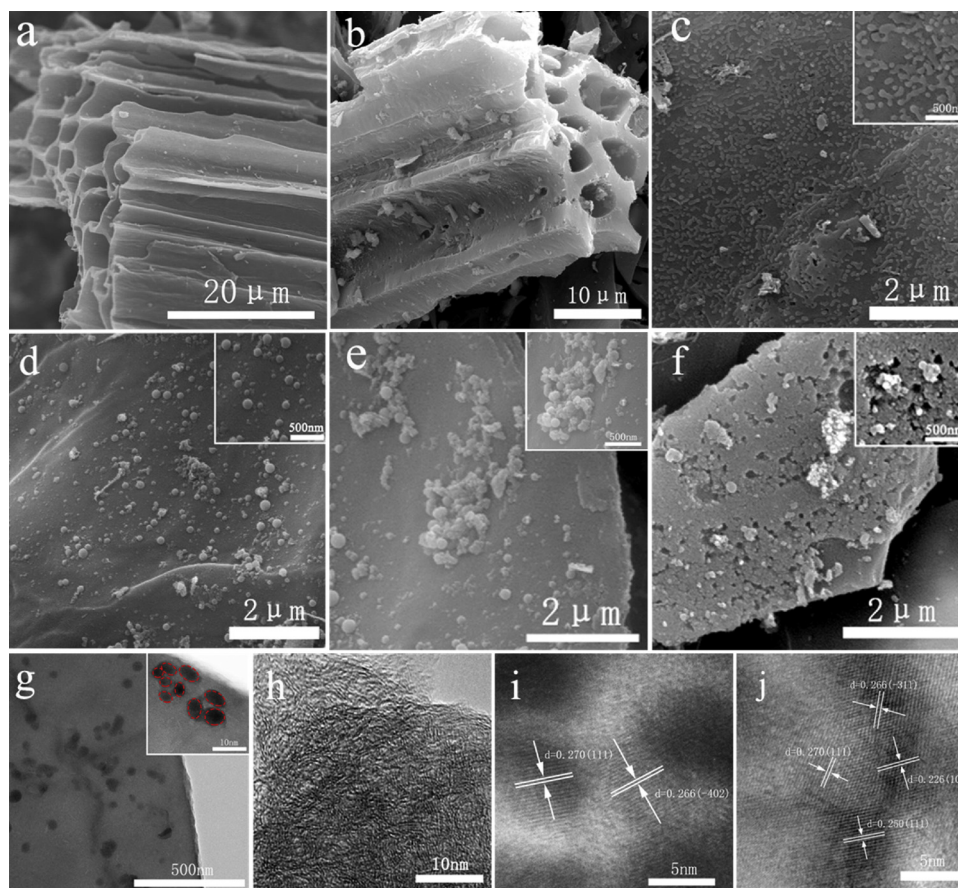**Fig. 3.** SEM images of cornstalk cores-derived carbon (a) and $Fe_3Se_4/FeSe/NPGC-x$ (x = 800 (c), 850 (b, d), 900 (e) and 950 (f)); TEM images of $Fe_3Se_4/FeSe/NPGC-850$ (g–j).

catalysts, consistent with XRD results. As shown in Fig. 2d and Fig. S2 (k–m), the peaks at around 55.9 and 58.8 eV correspond to Se $3d_{3/2}$ and Se $3d_{5/2}$, respectively [53,54]. It is confirmed that the valence state of Se in the $Fe_3Se_4/FeSe$ is -2.

As shown in Fig. 3a and b (SEM images), cornstalk cores still retain their original pore structure after carbonization. As shown in Fig. 3c–f, the surface of carbon support becomes unsmooth (a rugged (particles-coated) surface) after the Fe species are loaded. A large amount of particles (Fe species) are embedded in the carbon walls, which should act as the active sites to accelerate the ORR kinetics [43]. As temperature increases, the morphology of Fe species ($Fe_3Se_4/FeSe$) with different crystalline forms also changes on the carbon support. At 800 °C, the particles with short rod shape are uniformly (relatively) dispersed on the surface of carbon support. As shown in Fig. 3d, nearly monodisperse Fe species particles with spherical shape can be observed on the carbon surface. The well-dispersed particles should energetically increase the exposure of active sites on $Fe_3Se_4/FeSe$ to improve charge transfer efficiency in the ORR process. As shown in Fig. 3e, when the crystallization temperature is raised to 900 °C, the original uniformly-dispersed Fe species particles are severely aggregated. The stacking of particles may be mainly caused by the crystalline phase transition and the union (grain growth) of the $Fe_3Se_4/FeSe$. As shown in Fig. 3f, the iron species particles have undergone the un-desirable heating at 950 °C, which correspondingly provides the sufficient energy to cause the severe self-growth of $Fe_3Se_4/FeSe$. Moreover, the high temperature causes the collapse of carbon structure to clog the pore channels to decrease the specific surface area, which results in the decrease of exposed active sites and the deterioration of the diffusion and activation of O_2 molecules during the ORR.

TEM images of $Fe_3Se_4/FeSe/NPGC-850$ are shown in Fig. 3g–j.

Some nanoparticles with good dispersion are embedded in the structural skeleton of cornstalk cores-derived carbon (Fig. 3g). As shown in Fig. 3h, the introduction of Fe species can enhance the graphitization degree of carbon structure to improve the electrical conductivity of the catalyst, which makes the electron transfer easier during the ORR to thereby accelerate the reaction rate [35]. In high-resolution TEM (HRTEM) images of Fig. 3i and j, the measured crystalline lattice spacing of 0.270, 0.2663 and 0.2658 nm correspond to the (111), ($\bar{4}$ 02) and ($\bar{3}$ 11) crystal faces of Fe_3Se_4, respectively. As shown in Fig. 3j, the crystalline lattice spacing of 0.250 and 0.226 nm correspond to the (111) and (102) crystal planes of FeSe, respectively. Note that the crystal planes of FeSe obviously intersect with the crystal planes of Fe_3Se_4, indicating that $Fe_3Se_4/FeSe$ heterojunctions are formed in the $Fe_3Se_4/FeSe/NPGC-850$ and the mutual crystalline phase transition between Fe_3Se_4 and FeSe should be happened in the heterojunctions influenced by the carbonization temperature. The $Fe_3Se_4/FeSe$ heterojunctions embedded in the pore walls can provide a large number of active sites for ORR, which can greatly enhance the interface effects during the reaction [43,55]. In addition, because of the embedded structure and the mixed crystalline phase of $Fe_3Se_4/FeSe$, the catalyst is desirably stable and not easily aged (poisoned) during the ORR, which may thereby improve the volumetric efficiency and power output of the AC-MFC.

3.2. Performances of AC-MFCs with $Fe_3Se_4/FeSe/NPGC$ cathodes

The performances of AC-MFCs with $Fe_3Se_4/FeSe/NPGC$ and Pt/C cathodes are shown in Fig. 4. All of the reactors with the same carbon brush anodes are operated for 40 cycles (3 days per cycle). The highest voltages for each cycle are obtained to observe the changes in the
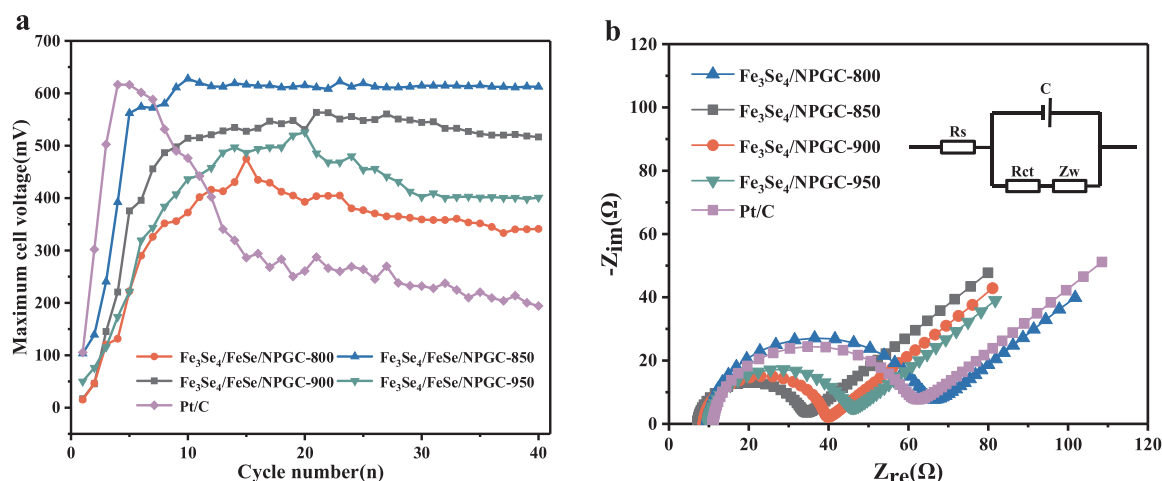
Fig. 4. (a) The maximum output voltage per cycle during operation of AC-MFCs with the five cathodes; (b) Nyquist curves and equivalent circuit diagrams during the operations (inset is the equivalent circuit).

voltage outputs of AC-MFCs with different cathodes. As shown in Fig. 4(a), the start-up of AC-MFC with Pt/C cathode is faster than others, which reaches the highest voltage output (616.6 mV) at the 4th cycle. However, the voltage of AC-MFC with Pt/C cathode gradually decreases from the 5th cycle until it is below 300 mV. This result indicates that Pt/C as a cathode has a poor bio-corrosion resistance in AC-MFCs. During the operation, the poisoning of Pt/C cathode should be caused by the attached electricity-generating microorganisms and the accumulation of metabolites in the electrolyte [56,57]. All of the voltage outputs of AC-MFCs with $Fe_3Se_4/FeSe/NPGC$ cathodes are more durable than that of Pt/C cathode in the 40 cycles' operation. The AC-MFC with $Fe_3Se_4/FeSe/NPGC$-850 cathode has the highest voltage output of 627.8 mV, which still remains 612.5 mV after 40 cycles, with a decline of only 2.4%. The porous structure of $Fe_3Se_4/FeSe/NPGC$-850 catalyst can greatly promote the permeation and diffusion of O_2 molecules in the cathode. The $Fe_3Se_4/FeSe$ heterojunctions as the main active components can greatly enhance the electron and proton transfer capacity, as well as the ORR activity and durability. The NiAs-type structure of Fe_3Se_4 with iron vacancies arranged in an ordered manner should contribute to the high catalytic activity and microbial resistance, so that the electron transfer pathway in ORR process is not easily affected by microorganisms [36]. Furthermore, FeSe nanoparticles embedded uniformly in NPGCs not only promote the charge transfer from $Fe_3Se_4/FeSe$ to carbon, but also enable the Fe more electrophilic, enhancing the ORR activity of $Fe_3Se_4/FeSe/NPGCs$ [39].

Fig. 4b shows the fitted Nyquist curves of AC-MFCs with the $Fe_3Se_4/FeSe/NPGC$ cathodes. The semicircular arc in the curves represents the charge transfer resistance (Rct), which indicates the difficulty of charge transfer in the actual operation by using the $Fe_3Se_4/FeSe/NPGC$ cathodes. The AC-MFC with the $Fe_3Se_4/FeSe/NPGC$-850 cathode has the lowest Rct of 25.07 Ω, while the $Fe_3Se_4/FeSe/NPGC$-800 cathode has the highest Rct of 51.95 Ω. Among them, the Rct values of $Fe_3Se_4/FeSe/NPGC$-850, $Fe_3Se_4/FeSe/NPGC$-900 and $Fe_3Se_4/FeSe/NPGC$-950 are all smaller than that of Pt/C (44.2 Ω). The efficient charge transfer of $Fe_3Se_4/FeSe/NPGC$-850 may be attributed to the smooth charge transfer pathways between $Fe_3Se_4/FeSe$ heterojunctions/N species and carbon support [55,56]. This result may be also ascribed to the part graphitization of the carbon support under high temperature pyrolysis, which can enhance the electrical conductivity of $Fe_3Se_4/FeSe/NPGC$ catalysts to make the charge transfer smoother.

Power density and electrode potential of the AC-MFCs are measured at the initial and final cycles (Fig. 5). Fig. 5a shows that AC-MFC with the $Fe_3Se_4/FeSe/NPGC$-850 cathode has the highest power density (1003 mW m^{-2}) and OCP (0.815 V), followed by $Fe_3Se_4/FeSe/NPGC$-900 (732 mW m^{-2}). The maximum power density (P_{MAX}) of $Fe_3Se_4/$

FeSe/NPGC-850 is higher than that of Pt/C (925 mW m^{-2}). Although Pt/C shows an acceptable performance at the initial cycle, its stability in AC-MFCs is not satisfactory. It shows that $Fe_3Se_4/FeSe/NPGC$-850 catalyst has higher electricity generation performance and bio-tolerance in AC-MFCs than those of Pt/C. As shown in Fig. 5b, the electrode potential change of the AC-MFCs is mainly concentrated on the cathode, and the potential change of the anode is not obvious (relatively). As shown in Fig. 5c, at the final cycle, power density of AC-MFC with $Fe_3Se_4/FeSe/NPGC$-850 cathode decreases by 7.8%, while Pt/C cathode decreases by 52.4%. A summary of the performances of MFCs (AC-MFC) with $Fe_3Se_4/FeSe/NPGC$-850 and other recently reported cathodes is illustrated in Table S2. The power density and voltage output stability of AC-MFC with $Fe_3Se_4/FeSe/NPGC$-850 cathode have obvious advantages compared with other catalysts. $Fe_3Se_4/FeSe/NPGC$-850 cathode receives little influence of microbial erosion on its ORR activity during the operation because the biofilm formation on cathode surface is inhibited by a small amount of H_2O_2 (or $\cdot OH$ and $\cdot O_2^-$ generated from the catalysis of H_2O_2) intermediate, which partly contributes to the fast ORR kinetics. After a long-term operation, microorganisms will generate a thick layer of biofilm on the surface of Pt/C cathode to suppress its ORR activity. The biofilm grown on the cathode surface will obstruct the electron transfer pathways of Pt/C cathode [43], thereby reducing the catalytic efficiency for ORR to decrease the power density and durability of AC-MFCs.

Fig. 6a shows the Tafel results tested in a neutral 50 mM PBS solution. As shown in Table 2, j_0 represents the exchange current density, which is an important parameter for evaluating the ORR performance of the catalyst in electrocatalytic tests. It is related to the concentration and free energy of the reactants at the equilibrium potential. Generally, the higher the j_0 is, the faster the charge transfer rate and the better the electrocatalytic activity are [58]. The fitting equations for the inset in Fig. 6a are shown in Table 2. It can be seen that j_0 of $Fe_3Se_4/FeSe/NPGC$-850 is greater than that of Pt/C, indicating that the charge transfer rate and ORR activity of $Fe_3Se_4/FeSe/NPGC$-850 is better than that of Pt/C at near equilibrium potential.

COD removal rate and CE for AC-MFCs with different cathodes are recorded over 20 cycles (Fig. 6b). Results show that the AC-MFC with $Fe_3Se_4/FeSe/NPGC$-850 cathode has the highest COD removal rate (average removal rate of 92.6%). The high COD removal rate can be attributed to the high ORR efficiency that occurs at the cathode of AC-MFC. As shown in Fig. 6b, the different CE values can be attributed to the different activities of electrogenic microorganisms on anodes, which are indirectly influenced by the different ORR catalytic activities of the cathode catalysts. AC-MFC with $Fe_3Se_4/FeSe/NPGC$-850 cathode obtains the highest CE among the five catalysts. The high ORR kinetics of
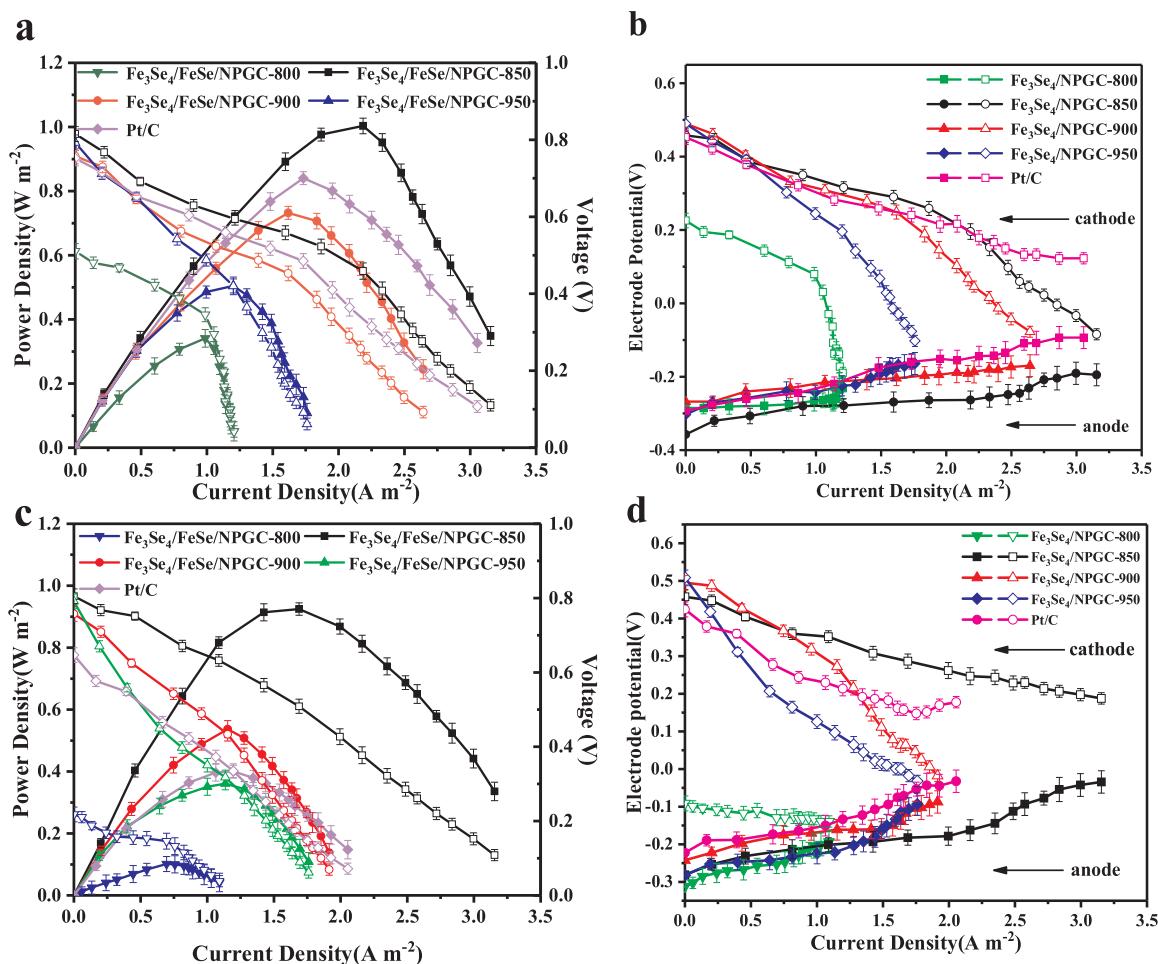
Fig. 5. Power density and the corresponding electrode potential of AC-MFCs (vs Ag/AgCl) with different cathodes as a function of current density at the initial (a and b) and final (c and d) cycles.

Fe_3Se_4/FeSe/NPGC-850 can energetically improve the biological tolerance of the cathode to make the electron transfer smooth and durable, thereby reducing the electron loss to improve CE and enhancing the bio-electricity generation activity of anodic microbes. Therefore, the high ORR activity of the Fe_3Se_4/FeSe/NPGC-850 cathode makes the AC-MFC have a stable power output and organic matter removal from wastewater.

Table 2
Linear fit equations and exchange current densities of the Tafel plots.

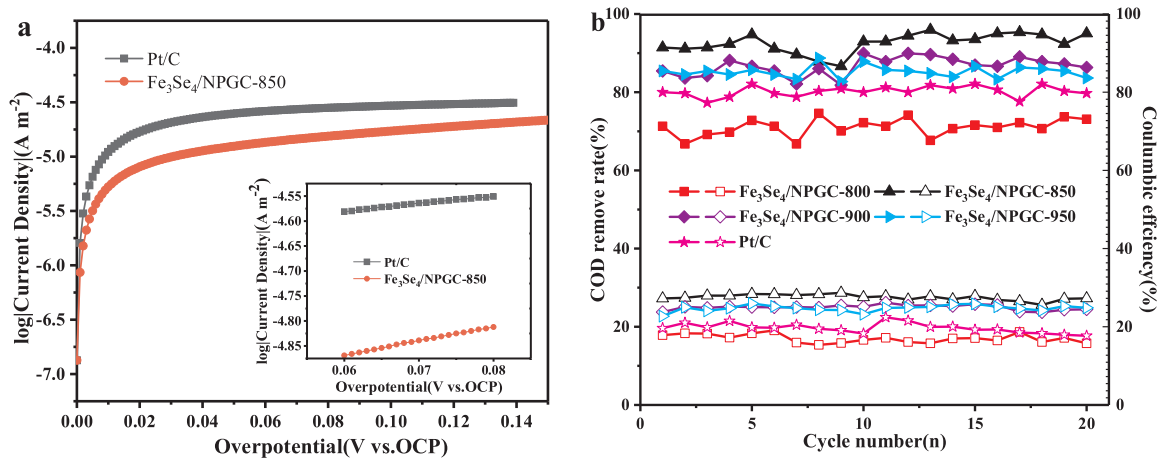| Samples	Fit linear equation	R^2	$10^{-4}j_0$ (A cm^{-2})
Pt/C	y = 1.440x-4.665	0.993	4.677
Fe_3Se_4/FeSe/NPGC-850	y = 2.846x-5.038	0.998	10.914

Fig. 6. (a) Tafel plots of all air cathodes (from open potential to over-potential with a scan rate of 1 mV s^{-1}) and linear fit for the Tafel plots (inset); (b) COD removal rate and CEs of AC-MFCs in each cycle.
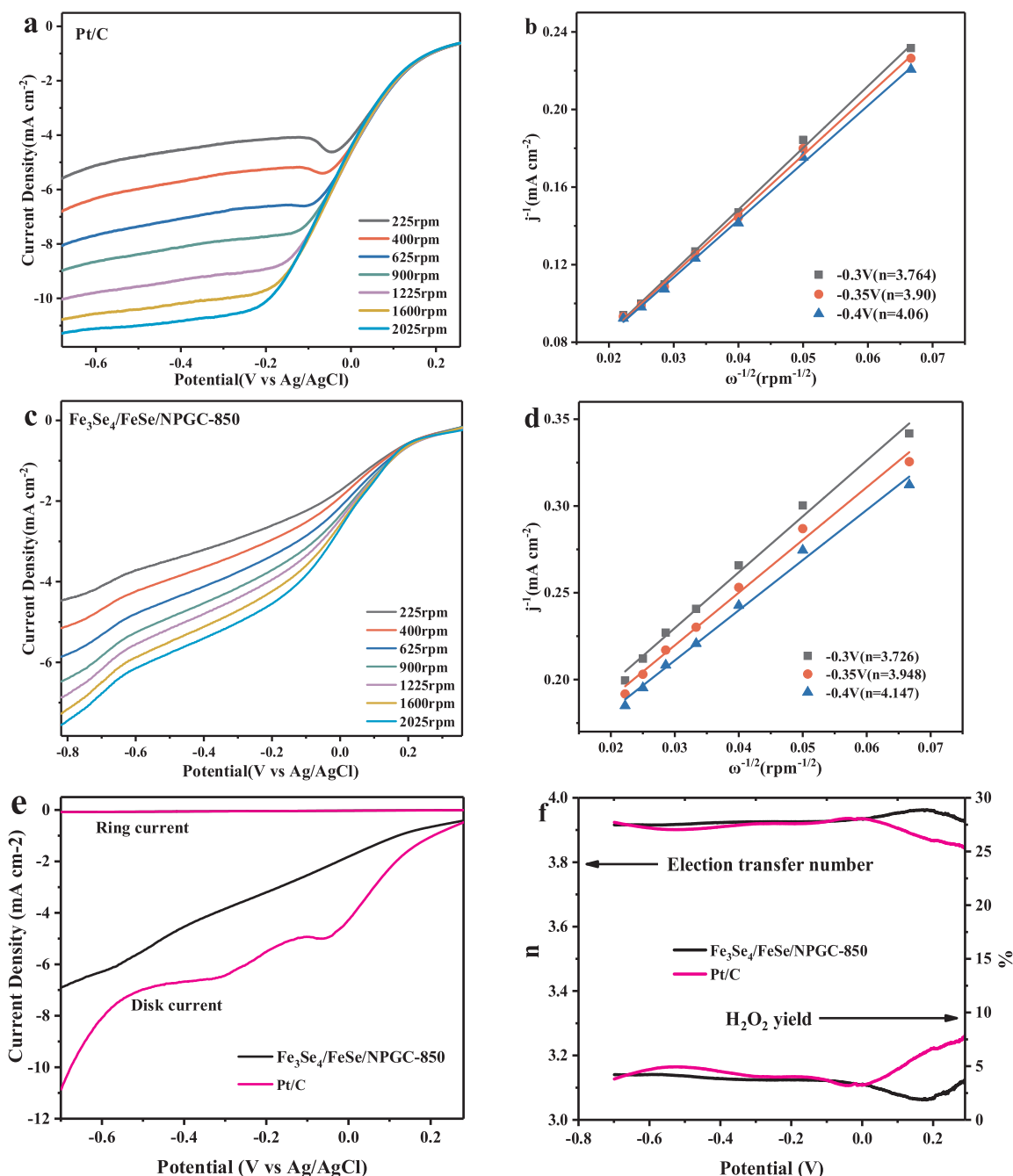
Fig. 7. RDE tests for (a) Pt/C and (c) Fe$_3$Se$_4$/FeSe/NPGC-850 at different rotating rates; Kouteckye-Levich plots of Fe$_3$Se$_4$/FeSe/NPGC-850 (b) and Pt/C (d); RRDE tests of the cathodic catalysts (e); Number of transferred electrons and the H$_2$O$_2$ yields (f).

3.3. Electrochemical tests for evaluating ORR activity of Fe$_3$Se$_4$/FeSe/NPGC-850

RDE tests for Fe$_3$Se$_4$/FeSe/NPGC-850 and Pt/C are conducted to evaluate their ORR activities (Fig. 7a–d). In Fig. 7b and 7d, the n values are calculated at the potentials of −0.3, −0.35, and −0.4 V. The K-L curves show a good linearity. The n values of Pt/C (n = 3.726, 3.948, 4.147) and Fe$_3$Se$_4$/FeSe/NPGC-850 (n = 3.764, 3.90, 4.06) are close to 4.0, indicating that their ORR processes are mainly conducted in the 4e$^-$ pathway with the low energy loss [18]. Fe$_3$Se$_4$/FeSe heterojunctions embedded in the pore channels can provide a large number of active sites for ORR, meanwhile the inherent pore channels of the cornstalks-derived carbon can promote the diffusion of the acceptor O$_2$ [49]. Moreover, the doped N-species (pyridinic N, pyrrolic N and

graphitic N) can also accelerate the ORR [19,49]. As reported previously, pyridinic N will activate the carbon atom in its ortho position, which can effectively reduce the O=O bond to thus promote the ORR catalytic activity [19]. Pyrrolic N can transfer a lone electron pair to carbon plane to generate the coordination sites to enhance the chemisorption of O$_2$ and ORR-related intermediates (H$_2$O$_2$, ·OH, ·O$_2^-$, etc) [49]. Graphitic N can further promote the electrical conductivity of PGC [49]. As previously reported, ORR activity can be significantly improved by the efficient charge transfer from the Fe$_3$Se$_4$/FeSe heterojunctions (or N species) to the NPGC [55]. Furthermore, N atoms coordinated in the carbon lattice can induce the formation of defects in carbon skeleton. The carbon defects also facilitate the charge transfer to improve ORR activity. Therefore, the synergistic effects among the iron selenides (Fe$_3$Se$_4$/FeSe), N species and porous structure are responsible

for the high ORR activity of Fe₃Se₄/FeSe/NPGCs.

RRDE measurements are performed for Fe₃Se₄/FeSe/NPGC-850 and Pt/C catalysts in O_2 saturated electrolytes to evaluate the number of transferred electrons as well as the H_2O_2 yield. As shown in Fig. 7e and f, both Fe₃Se₄/FeSe/NPGC-850 and Pt/C catalysts follow the $4e^-$ ORR pathway, consistent with the RDE results. In the potential range of -0.7 to 0.2 V, the H_2O_2 yields of both Pt/C and Fe₃Se₄/FeSe/NPGC-850 are less than 10%. It means that O_2 is dominantly reduced to H_2O on the Fe₃Se₄/FeSe/NPGC-850, which may be accompanied by a small proportion of two-step $2e^-$ pathway to generate a small amount of intermediates (H_2O_2, etc). It shows that the mesoporous structure of NPGC can make the catalyst to expose more active sites on the Fe₃Se₄/FeSe heterojunctions, which facilitate the charge and mass transfer to quickly eliminate the generated intermediates (H_2O_2, etc) during ORR. Therefore, the Fe₃Se₄/FeSe heterojunctions embedded in the NPGC skeleton with good electrical conductivity can act as the highly-active components due to their unique crystalline structure, which energetically promotes the charge transfer to enhance the activity and stability of ORR. As previously reported, the simultaneous introduction of Fe and Se not only facilitates the formation of N species (pyridinic N, pyrrolic N and graphitic N), but also obtains the coupling effects between Fe₃Se₄/FeSe and NPGCs to improve the ORR activity [39]. Furthermore, the formation of Fe₃Se₄/FeSe heterojunctions can efficiently decrease the overlapping of exposed (111), ($\bar{4}$ 02) and ($\bar{3}$ 11) crystal faces of Fe₃Se₄ to increase the iron vacancies in Fe₃Se₄ lattice to enhance the catalytic ORR activity of Fe₃Se₄ (or Fe₃Se₄/FeSe heterojunctions).

3.4. Deduction of ORR mechanisms for Fe₃Se₄/FeSe/NPGC catalysts in AC-MFCs

The catalyst layer in the air cathode of the AC-MFC is mainly consisted of Fe₃Se₄/FeSe/NPGCs. The high ORR efficiency and long-term stability of Fe₃Se₄/FeSe/NPGCs can be mainly attributed to the Fe₃Se₄/FeSe heterojunctions, the incorporation of heteroatoms N in PGC, and the active Fe₃Se₄ and FeSe particles. The N atoms doped in PGC cause a large number of defects in the carbon edges, making the active sites to be exposed [1,19]. Fe₃Se₄ and FeSe particles and Fe₃Se₄/FeSe heterojunctions in the NPGC framework can act as the highly-active components to accept the charges transferred from the anode. In addition, the efficiencies of permeation/diffusion, adsorption and dissociation of O_2 are also the important factors affecting the catalytic efficiency of Fe₃Se₄/FeSe/NPGCs [26]. Continuous O_2 molecules diffusion through the porous structure (pore channels) of NPGC can promote the oxygen adsorption and activation on the exposed active sites [11]. The active components in the carbon skeleton can energetically weaken the O−O bond to improve ORR activity. Therefore, O_2 diffused from the air cathode into AC-MFCs can more efficiently accept electrons from the external circuit to allow the ORR to occur smoothly. Due to the high ORR activity of Fe₃Se₄/FeSe/NPGCs, the cathode is not easily corroded by the electrogenic bacteria during the long-term operation. It can be concluded that the synergistic effects among the porous structure, the highly-active components (Fe₃Se₄/FeSe heterojunctions, pyridinic N, pyrrolic N and graphitic N), and the high electrically-conductive skeleton make the supply and dissociation of oxygen efficiently to enhance the long-term durability of AC-MFCs with Fe₃Se₄/FeSe/NPGC cathodes.

4. Conclusion

In summary, the Fe₃Se₄/FeSe/NPGCs are successfully prepared by using the cornstalk cores as the carbon source via a simple one-pot carbonization method. During the carbonization process, the crystal phase transition between Fe₃Se₄ and FeSe desirably occurs to form the Fe₃Se₄/FeSe heterojunctions. The high power density and voltage output of Fe₃Se₄/FeSe/NPGC-850 cathode for AC-MFCs can be attributed to the highly porous structure and active components in the NPGC

structure with high electrical conductivity. The porous structure can accelerate the mass transfer of O_2, while the doped N-species and Fe₃Se₄/FeSe heterojunctions can weaken the O − O bond to promote the consumption of O_2. In addition, the Fe₃Se₄/FeSe/NPGC-850 cathode also exhibits a higher stability than that of Pt/C after 120 d operation, indicating that the biological tolerance of Fe₃Se₄/FeSe/NPGC-850 with high ORR activity is much higher than that of Pt/C. It shows that the prepared Fe₃Se₄/FeSe/NPGC-850 catalyst with a high ORR activity and stability can be considered as a promising substitute for commercial Pt/C in AC-MFCs.

Appendix A. Supplementary data

Supplementary material related to this article can be found, in the online version, at doi:https://doi.org/10.1016/j.apcatb.2018.11.074.

References

[1] S. Li, C. Cheng, A. Thomas, Carbon-based microbial-fuel-cell electrodes: from conductive supports to active catalysts, Adv. Mater. 29 (2017) 1602547.

[2] M. Sun, L.F. Zhai, W.W. Li, H.Q. Yu, Harvest and utilization of chemical energy in wastes by microbial fuel cells, Chem. Soc. Rev. 45 (2016) 2847–2870.

[3] R. Rossi, W.L. Yang, E. Zikmund, D. Pant, B.E. Logan, In situ biofilm removal from air cathodes in microbial fuel cells treating domestic wastewater, Bioresour. Technol. 265 (2018) 200–206.

[4] H.M. Singh, A.K. Pathak, K. Chopra, V.V. Tyagi, S. Anand, R. Kothari, Microbial fuel cells: a sustainable solution for bioelectricity generation and wastewater treatment, Biofuels 1 (2018) 1–21.

[5] L. Zhou, C.M. Liao, T. Li, J.K. An, Q. Du, L.L. Wan, N. Li, X.Q. Pan, X. Wang, Regeneration of activated carbon air-cathodes by half-wave rectified alternating fields in microbial fuel cells, Appl. Energy 219 (2018) 199–206.

[6] L. He, P. Du, Y.Z. Chen, H.W. Lu, X. Cheng, B. Chang, Z. Wang, Advances in microbial fuel cells for wastewater treatment, Renew. Sustain. Energy Rev. 71 (2017) 388–403.

[7] B.C. Wang, J. Du, X.F. Chen, A.W. Thomas, N.D. Kirchhofer, L.E. Garner, M.T. Maw, W.H. Poh, J. Hinks, S. Wuertz, S. Kjelleberg, Q.C. Zhang, J.S.C. Loo, G.C. Bazan, Improving charge collection in Escherichia coli-carbon electrode devices with conjugated oligoelectrolytes, Phys. Chem. Chem. Phys. 15 (2013) 5867–5872.

[8] R.B. Song, Y.C. Wu, Z.Q. Lin, J. Xie, C.H. Tan, J.S.C. Loo, B. Cao, J.R. Zhang, J.J. Zhu, Q.C. Zhang, Angew. Chem. Int. Ed. 56 (2017) 10516–10520.

[9] B.E. Logan, B. Hamelers, R. Rozendal, U. Schröder, J. Keller, S. Freguia, P. Aelterman, W. Verstraete, K. Rabaey, Microbial fuel cells: methodology and technology, Environ. Sci. Technol. 40 (2006) 5181–5192.

[10] C.E. Zhao, J.S.H. Wu, S. Kjelleberg, J.S.C. Loo, Q.C. Zhang, Employing a flexible and low-cost polypyrrole nanotube membrane as an anode to enhance current generation in microbial fuel cells, Small 28 (2015) 3440–3443.

[11] L. Yang, Z. Cai, L. Hao, Z.P. Xing, Y. Dai, X. Xu, S.Y. Pan, Y.Q. Duan, J.L. Zou, Nano Ce₂O₂S with highly enriched oxygen-deficient Ce³⁺ sites supported by N and S dual-doped carbon as an active oxygen supply catalyst for the oxygen reduction reaction, ACS Appl. Mater. Interfaces 9 (2017) 22518–22529.

[12] M.K. Sarma, M.G.A. Quadir, R. Bhaduri, S. Kaushik, P. Goswami, Composite polymer coated magnetic nanoparticles based anode enhances dye degradation and power production in microbial fuel cells, Biosens. Bioelectron. 119 (2018) 94–102.

[13] C.E. Zhao, P.P. Gai, R.B. Song, Y. Chen, J.R. Zhang, J.J. Zhu, Nanostructured material-based biofuel cells: recent advances and future prospects, Chem. Soc. Rev. 46 (2017) 1545–1564.

[14] B. Mecheri, V.C.A. Ficca, M.A.C. Oliveira, A. D'Epifanio, E. Placidi, F. Arciprete, S. Licoccia, Facile synthesis of graphene-phthalocyanine composites as oxygen reduction electrocatalysts in microbial fuel cells, Appl. Catal. B 237 (2018) 699–707.

[15] H.L. Tang, Y. Zeng, Y.X. Zeng, R. Wang, S.C. Cai, C. Liao, H.P. Cai, X.H. Lu, P. Tsiakaras, Iron-embedded nitrogen doped carbon frameworks as robust catalyst for oxygen reduction reaction in microbial fuel cells, Appl. Catal. B 202 (2017) 550–556.

[16] Z.Y. Fa, J. Li, Y. Zhou, Q. Fu, W. Yang, X. Zhu, Q. Liao, A green, cheap, high-performance carbonaceous catalyst derived from chlorella pyrenoidosa for oxygen reduction reaction in microbial fuel cells, Int. J. Hydrogen Energy 42 (2017) 27657–27665.

[17] T.H. Han, N. Parveen, J.H. Shim, A.T.N. Nguyen, N. Mahato, M.H. Cho, Ternary composite of polyaniline graphene and TiO_2 as a bifunctional catalyst to enhance the performance of both the bioanode and cathode of a microbial fuel cell, Ind. Eng. Chem. Res. 57 (2018) 6705–6713.

[18] C. Santoro, A. Serov, L. Stariha, M. Kodali, J. Gordon, S. Babanova, O. Bretschger, K. Artyushkova, P. Atanassov, Iron based catalysts from novel low-cost organic precursors for enhanced oxygen reduction reaction in neutral media microbial fuel cells, Energy Environ. Sci. 9 (2016) 2346–2353.

[19] C.R. Raj, A. Samanta, S.H. Noh, S. Mondal, T. Okajimab, T. Ohsaka, Emerging new generation electrocatalysts for the oxygen reduction reaction, J. Mater. Chem. A 4 (2016) 11156–11178.

[20] R. Kumar, L. Singh, A.W. Zularisam, Enhanced oxygen reduction reaction in air-cathode microbial fuel cells using flower-like Co_3O_4 as an efficient cathode catalyst, Int. J. Hydrogen Energy 42 (2017) 19287–19295.

[21] K.Y. Chen, X.B. Huang, C.Y. Wand, H. Liu, Efficient oxygen reduction catalysts formed of cobalt phosphide nanoparticle decorated heteroatom-doped mesoporous carbon nanotubes, Chem. Commun. 51 (2015) 7891–7894.

[22] C. Santoro, A. Serov, R. Gokhale, S. Rojas-Carbonell, L. Stariha, J. Gordon, K. Artyushkova, P. Atanassov, A family of Fe-N-C oxygen reduction electrocatalysts for microbial fuel cell (MFC) application: relationships between surface chemistry and performances, Appl. Catal. B 205 (2017) 24–33.

[23] R.B. Song, K. Yan, Z.Q. Lin, J.S.C. Loo, L.J. Pan, Q.C. Zhang, J.R. Zhang, J.J. Zhu, Inkjet-printed porous polyaniline gel as an efficient anode for microbial fuel cells, J. Mater. Chem. A 4 (2016) 14555–14559.

[24] X.J. Wang, H.G. Zhang, H.H. Lin, S. Gupta, C. Wang, Z.X. Tao, H. Fu, T. Wang, J. Zheng, G. Wu, X.G. Li, Directly converting Fe-doped metal–organic frameworks into highly active and stable Fe-N-C catalysts for oxygen reduction in acid, Nano Energy 25 (2016) 110–119.

[25] M.M. Hossen, K. Artyushkova, P. Atanassov, A. Serov, Synthesis and characterization of high performing Fe-N-C catalyst for oxygen reduction reaction (ORR) in alkaline exchange membrane fuel cells, J. Power Sources 375 (2018) 214–221.

[26] L. Hao, J. Yu, X. Xu, L. Yang, Z.P. Xing, Y. Dai, Y. Sun, J.L. Zou, Nitrogen-doped MoS_2/carbon as highly oxygen-permeable and stable catalysts for oxygen reduction reaction in microbial fuel cells, J. Power Sources 339 (2017) 68–79.

[27] Z.H. Wen, S.Q. Ci, F. Zhang, X.L. Feng, S.M. Cui, Sh. Mao, Sh.L. Luo, Z. He, J.H. Chen, Nitrogen-enriched core-shell structured Fe/Fe3C-C nanorods as advanced electrocatalysts for oxygen reduction reaction, Adv. Mater. 24 (2012) 1399–1404.

[28] C.H. Ding, J.J. Tang, S. Chen, Z.Q. Liu, N. Li, $Co_{0.85}Se$/multi-walled carbon nanotube composite as alternative cathode catalyst for microbial fuel cells, J. Nanosci. Nanotechnol. 17 (2017) 1438–1442.

[29] A. Serov, K. Artyushkova, P. Atanassov, Fe-N-C oxygen reduction fuel cell catalyst derived from carbendazim: synthesis, structure, and reactivity, Adv. Energy Mater. 4 (2014) 1301735.

[30] X.G. Fu, Y.R. Liu, X.P. Cao, J.T. Jin, Q. Liu, J.Y. Zhang, FeCo–Nx embedded graphene as high performance catalysts for oxygen reduction reaction, Appl. Catal. B 130–131 (2013) 143–151.

[31] A. Aijaz, J. Masa, C. Rçsler, W. Xia, P. Weide, A.J.R. Botz, R.A. Fischer, W. Schuhmann, M. Muhler, Co@Co3O4 encapsulated in carbon nanotube-grafted nitrogen doped carbon polyhedra as an advanced bifunctional oxygen electrode, Angew. Chem. Int. Ed. 55 (2016) 4087–4091.

[32] J.W. Ren, M. Antonietti, T.P. Fellinger, Efficient water splitting using a simple Ni/N/C paper electrocatalyst, Adv. Energy Mater. 5 (2015) 1401660.

[33] X.X. Zhou, Y.Z. Xu, X.J. Mei, N.J. Du, R.M. Jv, Z.X. Hu, S.W. Chen, Polyaniline/β-MnO_2 nanocomposites as cathode electrocatalyst for oxygen reduction reaction in microbial fuel cells, Chemosphere 198 (2018) 482–491.

[34] X. Xu, Y. Dai, J. Yu, L. Hao, Y.Q. Duan, Y. Sun, Y.H. Zhang, Y.H. Lin, J.L. Zou, Metallic state FeS anchored (Fe)/Fe3O4/N-doped graphitic carbon with porous spongelike structure as durable catalysts for enhancing bioelectricity generation, ACS Appl. Mater. Interfaces 9 (2017) 10777–10787.

[35] Y. Lv, Y.H. Lin, L. Yang, Zh. Cai, B.J. Jing, J. Yu, X.K. Jiang, Z.P. Xing, J.L. Zou, Iron (III) metaphosphate/iron phosphide heterojunctions embedded in partly-graphitized carbon for enhancing charge transfer and power generation in microbial fuel cells, Chem. Eng. J. 342 (2018) 228–237.

[36] K. Hirakawa, The magnetic properties of iron selenide single crystals, J. Phys. Soc. Jpn. 12 (1957) 929–938.

[37] M.S. Bishwas, R. Das, P. Poddar, Large increase in the energy product of Fe_3Se_4 by Fe-site doping, J. Phys. Chem. C 118 (2014) 4016–4022.

[38] Q. Ma, Q. Zhuang, H. Song, C. Zhao, Z. Zhang, J. Liu, H. Peng, C. Mao, G. Li, Large-scale synthesis of Fe_3Se_4/C composites assembled by aligned nanorods as advanced anode material for lithium storage, Mater. Lett. 228 (2018) 235–238.

[39] G. Wang, J. Li, M. Liu, L. Du, S. Liao, Three-dimensional biocarbon framework coupled with uniformly distributed FeSe nanoparticles derived from pollen as bi-functional electrocatalysts for oxygen electrode reactions, Appl. Mater. Interfaces 10 (2018) 32133–32141.

[40] H. Dong, H.B. Yu, X. Wang, Catalysis kinetics and porous analysis of rolling acti-vated carbon PTFE air-cathode in microbial fuel cells, Environ. Sci. Technol. 46 (2012) 13009–13015.

[41] H. Dong, H.B. Yu, X. Wang, Q.X. Zhou, J.L. Feng, A novel structure of scalable air-cathode without nafion and Pt by rolling activated carbon and PTFE as catalyst layer in microbial fuel cells, Water Res. 46 (2012) 5777–5787.

[42] C.E. Zhao, J.S. Wu, Y.Z. Ding, V.B. Wang, Y.D. Zhang, S. Kjelleberg, J.S.C. Loo, B. Cao, Q.C. Zhang, Hybrid conducting biofilm with built-in bacteria for high performance microbial fuel cells, ChemElectroChem 2 (2015) 654–658.

[43] Y.Z. Chan, Y. Dai, R. Li, J.L. Zou, G.H. Tian, H.G. Fu, Low-temperature synthesized nitrogen-doped iron/iron carbide/partly-graphitized carbon as stable cathode cat-alysts for enhancing bioelectricity generation, Carbon 89 (2015) 8–19.

[44] S.Y. Pan, Z. Cai, Y.Q. Duan, L. Yang, B. Tang, B.J. Jing, Y. Dai, X. Xu, J.L. Zou, Tungsten diselenide/porous carbon with sufficient active edge-sites as a co-cata-lyst/Pt-support favoring excellent tolerance to methanol-crossover for oxygen re-duction reaction in acidic medium, Appl. Catal. B 219 (2017) 18–29.

[45] C. Santoro, R. Gokhale, B. Mecheri, A. D'Epifanio, S. Licoccia, A. Serov, K. Artyushkova, P. Atanassov, Design of iron(II) pthalocyanine (FePc) derived oxygen reduction electrocatalysts for high power density microbial fuel cells, ChemSusChem 10 (2017) 3243–3251.

[46] H.W. Zhang, G. Long, D. Li, R. Sabirianov, H. Zeng, Fe_3Se_4 nanostructures with giant coercivity synthesized by solution chemistry, Chem. Mater. 23 (2011) 3769–3774.

[47] A.K. Dutta, S.K. Maji, D.N. Srivastava, A. Mondal, P. Biswas, P. Paul, B. Adhikary, Synthesis of FeS and FeSe nanoparticles from a single source srecursor: a study of their photocatalytic activity, peroxidase-like behavior, and electrochemical sensing of H_2O_2, ACS Appl. Mater. Interfaces 4 (2012) 1919–1927.

[48] R. Schmidt, M. Stocker, E. Hansen, D. Akporiaye, O.H. Ellestad, MCM-41: a model system for adsorption studies on mesoporous materials, Microporous Mater. 3 (1995) 443–448.

[49] Y. Sun, Y.Q. Duan, L. Hao, Z.P. Xing, Y. Dai, R. Li, J.L. Zou, Cornstalk-derived nitrogen-doped partly graphitized carbon as efficient metal-free catalyst for oxygen reduction reaction in microbial fuel cells, ACS Appl. Mater. Interfaces 8 (2016) 25923–25932.

[50] H.L. Peng, Z.Y. Mo, S.J. Liao, H.G. Liang, L.J. Yang, F. Luo, H.Y. Song, Y.L. Zhong, B.Q. Zhang, High performance Fe- and N- doped carbon catalyst with graphene structure for oxygen reduction, Sci. Rep. 1765 (2013) 1–7.

[51] A.H. Battez, R. González, J.L. Viesca, D. Blanco, E. Asedegbega, A. Osorio, Tribological behaviour of two imidazolium ionic liquids as lubricant additives for steel/steel contacts, Wear 266 (2009) 1224–1228.

[52] P.J. Yao, J. Wang, H.Y. Du, J.Q. Qi, Synthesis, characterization and formaldehyde gas sensitivity of $La_{0.7}Sr_{0.3}FeO_3$ nanoparticles assembled nanowires, Mater. Chem. Phys. 134 (2012) 61–67.

[53] R. Goyal, R. Gupta, A.K. Srivastava, V.P.S. Awana, Superconductivity at 5.5 K in Nb_2PdSe_5 compound, J. Supercond. Nov. Magn. 26 (2016) 2705–2710.

[54] P.V. Galiy, A.V. Musyanovych, Y.M. Fiyala, The interface microscopy and spec-troscopy on the cleavage surfaces of the In_4Se_3 pure and copper-intercalated layered crystals, Phys. E 35 (2006) 88–92.

[55] Y. Zheng, T.F. Zhou, C.F. Zhang, J.F. Mao, H.K. Liu, Z.P. Guo, Boosted charge transfer in SnS/SnO_2 heterostructures: toward high rate capability for sodium-ion batteries, Angew. Chem. 55 (2016) 3408–3413.

[56] C. Santoro, A. Stadlhofer, V. Hacker, G. Squadrito, U. Schröder, B.K. Li, Activated carbon nanofibers (ACNF) as cathode for single chamber microbial fuel cells (SCMFCs), J. Power Sources 243 (2013) 499–507.

[57] F. Harnisch, U. Schröder, From MFC to MXC: chemical and biological cathodes and their potential for microbial bioelectrochemical systems, Chem. Soc. Rev. 39 (2010) 4433–4448.

[58] H. Dong, H.B. Yu, X. Wang, Q.X. Zhou, J.W. Sun, Carbon-supported perovskite oxides as oxygen reduction reaction catalyst in single chambered microbial fuel cells, J. Chem. Technol. Biotechnol. 88 (2013) 774–778.